

3D Optical Coherence Thermometry Using Polymeric Nanogels

Tamara Muñoz-Ortiz, Idoia Alayeto, José Lifante, Dirk H. Ortgies, Riccardo Marin, Emma Martín Rodríguez, María del Carmen Iglesias de la Cruz, Ginés Lifante-Pedrola, Jorge Rubio-Retama,* and Daniel Jaque*

In nanothermometry, the use of nanoparticles as thermal probes enables remote and minimally invasive sensing. In the biomedical context, nanothermometry has emerged as a powerful tool where traditional approaches, like infrared thermal sensing and contact thermometers, fall short. Despite the strides of this technology in preclinical settings, nanothermometry is not mature enough to be translated to the bedside. This is due to two major hurdles: the inability to perform 3D thermal imaging and the requirement for tools that are readily available in the clinics. This work simultaneously overcomes both limitations by proposing the technology of optical coherence thermometry (OCTh). This is achieved by combining thermoresponsive polymeric nanogels and optical coherence tomography (OCT)—a 3D imaging technology routinely used in clinical practice. The volume phase transition of the thermoresponsive nanogels causes marked changes in their refractive index, making them temperature-sensitive OCT contrast agents. The ability of OCTh to provide 3D thermal images is demonstrated in tissue phantoms subjected to photothermal processes, and its reliability is corroborated by comparing experimental results with numerical simulations. The results included in this work set credible foundations for the implementation of nanothermometry in the form of OCTh in clinical practice.

1. Introduction

Monitoring and controlling deep body temperature is a key issue in biomedicine. In recent years, new diagnostic methods based on precise thermometry have emerged allowing early diagnosis of tumors, inflammation, detection of ischemic events, and alterations in brain activity.^[1] Precise and real-time monitoring of temperature also made possible the minimization of collateral damage during the thermal treatment of tumors.^[2] For these applications, the temperature must be determined in a remote way in order to minimize stress and avoid behavioral alterations in the individual. Diverse technologies have proven capable of remote thermal monitoring in vivo, including microwave thermometry,^[3] ultrasound thermometry,^[4] fluorescence thermometry,^[5] and functional magnetic resonance imaging.^[6] In Section S1 (Supporting Information) we include a comparative table of the most employed biomedical thermographic techniques. To date, the only technology capable of


T. Muñoz-Ortiz, D. H. Ortgies, R. Marin, G. Lifante-Pedrola, D. Jaque
nanomaterials for BioImaging Group (nanoBIG)
Departamento de Física de Materiales
Facultad de Ciencias
Universidad Autónoma de Madrid
C/ Francisco Tomás y Valiente 7, Madrid 28049, Spain
E-mail: daniel.jaque@uam.es
T. Muñoz-Ortiz, D. H. Ortgies, R. Marin, E. Martín Rodríguez, D. Jaque
Instituto Nicolás Cabrera
Facultad de Ciencias
Universidad Autónoma de Madrid
C/ Francisco Tomás y Valiente 7, Madrid 28049, Spain

I. Alayeto, J. Rubio-Retama
Departamento de Química en Ciencias Farmacéuticas
Facultad de Farmacia
Plaza de Ramón y Cajal
s/n
Universidad Complutense de Madrid
Madrid 28040, Spain
E-mail: bjrubio@ucm.es

J. Lifante, M. del C. Iglesias de la Cruz
nanomaterials for BioImaging Group (nanoBIG)
Departamento de Fisiología
Facultad de Medicina
Universidad Autónoma de Madrid
Avda. Arzobispo Morcillo 2, Madrid 28029, Spain

J. Lifante, D. H. Ortgies, E. Martín Rodríguez, J. Rubio-Retama, D. Jaque
nanomaterials for BioImaging Group (nanoBIG)
Instituto Ramón y Cajal de Investigación Sanitaria
Ctra de Colmenar Viejo Km 9, 100, Madrid 28034, Spain

E. Martín Rodríguez
Institute for Advanced Research in Chemical Sciences (IAdChem)
Universidad Autónoma de Madrid
Madrid 28049, Spain

 The ORCID identification number(s) for the author(s) of this article can be found under <https://doi.org/10.1002/adma.202301819>

© 2023 The Authors. Advanced Materials published by Wiley-VCH GmbH. This is an open access article under the terms of the Creative Commons Attribution License, which permits use, distribution and reproduction in any medium, provided the original work is properly cited.

DOI: 10.1002/adma.202301819

3D thermal imaging in animal models is MRI.^[7] Although successfully applied for thermal monitoring of glioblastoma treatments, MRI lacks real-time capabilities and requires sophisticated and expensive apparatus that limits its daily use in clinics.^[8] The rest of the abovementioned technologies with possibilities of being translated into clinics are only capable of 2D thermal imaging, which prevents, for example, the study of heat diffusion or the accurate location of spatial thermal singularities within tissues. This is of special importance when dealing with organs such as the brain, where relevant thermal differences between different locations are expected due to its inhomogeneous activity.^[9] The real-time acquisition of 3D thermal images remains a technological challenge that cannot be credibly tackled with the materials and techniques developed so far.

Optical coherence tomography (OCT) is a widely used clinical interferometric technique capable of 3D structural imaging of tissues in real-time. Although OCT was initially used exclusively in ophthalmology,^[10] nowadays it is used in other fields such as cardiology, brain imaging, tissue analysis, and dermatology.^[11] In the past years, the combination of OCT with nanoparticles has further enhanced its sensitivity and has allowed 3D molecular imaging of tissues and cells.^[12] The ability of nanoparticle-assisted OCT to provide 3D images of tissues makes it a suitable platform to develop 3D thermometry approaches. To do so, OCT should be combined with optical probes whose scattering properties are strongly dependent on temperature. In this context, thermo-responsive nanogels (NGs) like poly(*N*-isopropylacrylamide) (PNIPAM) are a viable option due to their capacity to undergo volume phase transitions in aqueous dispersions as a response to small changes in the environmental temperature, as represented in **Figure 1**. When the temperature is above the lower critical solution temperature (LCST), PNIPAM-NGs suffer an abrupt and marked reduction of their hydrodynamic diameter due to the collapse of the polymer chains. This process is accompanied by the expulsion of most of the water molecules, leading to an increase in density and refractive index.^[13] Considering that the OCT signal is refractive-index dependent, we envisioned that this temperature-dependent behavior of PNIPAM-NGs could be harnessed to achieve 3D optical coherence thermometry (OCTh).

2. Results and Discussion

In this work, we have explored the combination of PNIPAM-NGs and OCT for 3D thermal imaging of tissues by OCTh. PNIPAM-NGs were selected because of their thermoresponsive behavior and, not less importantly, because they are one of the polymeric systems most extensively studied for biomedical applications

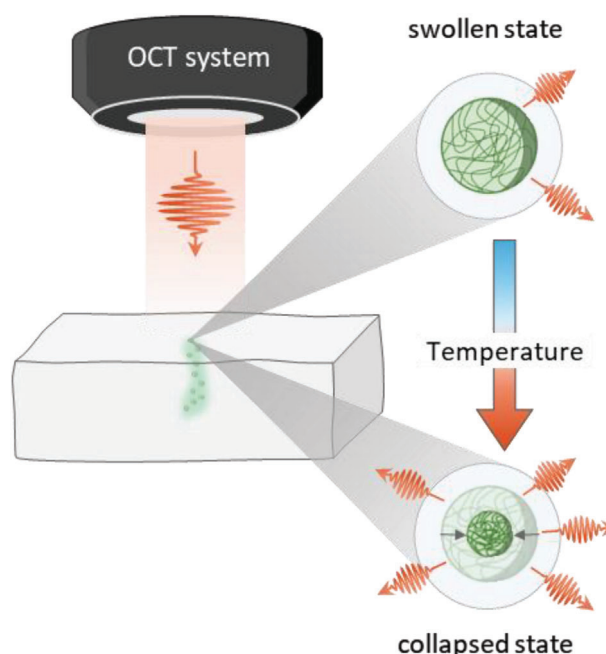


Figure 1. Schematic representation of the temperature-dependent response of PNIPAM-NGs in OCT. When the NGs are above the LCST, their increase in refractive index yields a stronger scattering signal.

like treatment of solid tumors, selective drug delivery, and controlled cell attachment/detachment.^[14] Recent works report that PNIPAM-NGs show reduced cytotoxicity in HeLa and breast cancer cells.^[15] Moreover, we tested the cytotoxicity of our PNIPAM-NGs in a non-tumoral cell line such as human microvasculature endothelial cells. The results included in Section S2 (Supporting Information) indicate that, after 24 h of incubation with different concentrations of PNIPAM-NGs dispersed in culture medium, the cell viability is in all the cases superior to 70%, and therefore the NGs can be considered non-cytotoxic.

The PNIPAM-NGs used in this work have been prepared according to the method described in the Experimental Section. They show a spherical shape (**Figure 2a**) with a hydrodynamic diameter that decreases from 284 to 168 nm when the temperature increases from 25 to 50 °C (**Figure 2b**). The temperature dependence of the hydrodynamic diameter ($D(T)$) can be described by a four-parameter sigmoidal function:^[16]

$$D(T) = D_{\min} + \frac{D_{\max} - D_{\min}}{1 + \exp\left(\frac{T - \text{LCST}}{\tau}\right)} \quad (1)$$

where $D_{\min} = 168 \pm 1$ nm, and $D_{\max} = 284 \pm 4$ nm are the minimum and maximum hydrodynamic diameters, (i.e., in the collapsed and swollen states respectively), $\text{LCST} = 33.8 \pm 0.2$ °C is the volume phase transition temperature, and $\tau = 1.5 \pm 0.2$ °C is the temperature half-width of the transition. The Z-potential of the PNIPAM-NGs dispersed in phosphate buffer was evaluated for different pH values, obtaining a value close to −11 mV in all cases (see Section S3, Supporting information). To evaluate the potential of the PNIPAM-NGs as scattering units

D. H. Ortgies, R. Marin, E. Martín Rodríguez, D. Jaque
nanomaterials for BioImaging Group (nanoBIG)
Departamento de Física Aplicada
Facultad de Ciencias
Universidad Autónoma de Madrid
Madrid 28049, Spain

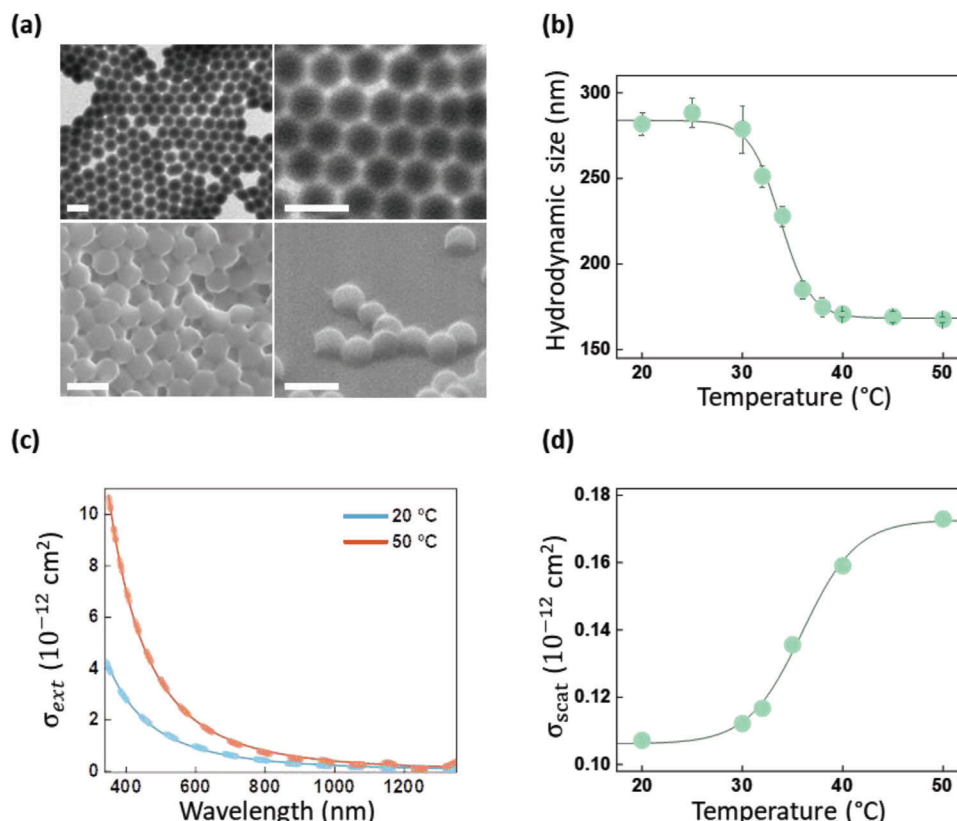


Figure 2. a) TEM (top) and SEM (bottom) images of the PNIPAM-NGs. Scale bars: 500 nm. b) Temperature dependence of the hydrodynamic diameter of the PNIPAM-NGs. Dots are experimental data and the solid line is the best fit to a four-parameter sigmoidal function (Equation (1)). The error bars correspond to the standard deviation of the maximum of the three measured size distributions. c) Extinction cross-section spectra of a colloidal dispersion of PNIPAM-NGs (2.7 mg mL^{-1}) at temperatures below (20°C) and above (50°C) the LCST. Dashed lines are experimental data, and solid lines are the best fit to the $1/\lambda^n$ trend. d) Temperature dependence of the scattering cross section of the colloidal dispersion of PNIPAM-NGs at 1300 nm (OCT operation wavelength). Dots are experimental data, and the solid line is the best fit to a four-parameter sigmoidal function.

(i.e., OCT contrast agents), their extinction cross section (σ_{ext}) was determined for different temperatures (see Figure 2c, Section S4, Supporting Information). The $\sigma_{ext}(\lambda)$ curves were found to fit well to a $1/\lambda^n$ trend with n varying between 2.8 and 3.1 depending on the temperature (see Section S4, Supporting Information). $n \approx 3$ reveals that PNIPAM-NGs can be approximately described as non-absorbing Rayleigh scattering units. This occurs when the particle size is much smaller than the wavelength of the incident light, a condition fully satisfied at the OCT operation wavelength (1300 nm). The absence of absorption ($\sigma_{abs} \ll \sigma_{scat}$) allows to determine the scattering cross section (σ_{scat}) since $\sigma_{ext} = \sigma_{abs} + \sigma_{scat} \approx \sigma_{scat}$. Experimental data reveal that the scattering cross section of PNIPAM-NGs at the OCT operating wavelength ($\sigma_{scat}(1300 \text{ nm})$) increases with temperature following a four-parameter sigmoidal function (Figure 2d) with an LCST close to $34.3 \pm 0.3^\circ\text{C}$, in good agreement with the values obtained from the fit of the hydrodynamic diameter (Figure 2b). Such agreement reveals the unequivocal relationship between the scattering cross section of PNIPAM-NGs and their structural phase transition. As a first-order approximation, the Rayleigh formalism used to describe photon scattering can be used to elucidate the physical mechanism behind the increase of

the refractive index caused by the collapse of the polymer chains. The scattering cross section of a Rayleigh particle surrounded by water can be written as:

$$\sigma_{scat} = \frac{2\pi^5}{3} \frac{D^6}{\lambda^4} \left(\frac{n_p^2 - 1.33^2}{n_p^2 + 1.33^2} \right)^2 \quad (2)$$

where D is the particle diameter and n_p is the refractive index of the particle. The collapse of PNIPAM-NGs yields a reduction in their size that reduces their scattering cross section (term D^6 in Equation (2)). At the same time, the volume phase transition causes an increase in the refractive index of the PNIPAM-NGs that tends to increase its scattering cross section (term $\left(\frac{n_p^2 - 1.33^2}{n_p^2 + 1.33^2}\right)^2$ in Equation (2)). Since the experimental data reveal an increase in the scattering cross section it can be concluded that the change in the refractive index due to the collapse of the polymer dominates over the size reduction in the overall scattering properties of the PNIPAM-NGs.

The room-temperature (20°C) scattering cross section of the PNIPAM-NGs at 1300 nm is $1.1 \times 10^{-13} \text{ cm}^2$. This is two orders of magnitude smaller than the one of gold nanoshells

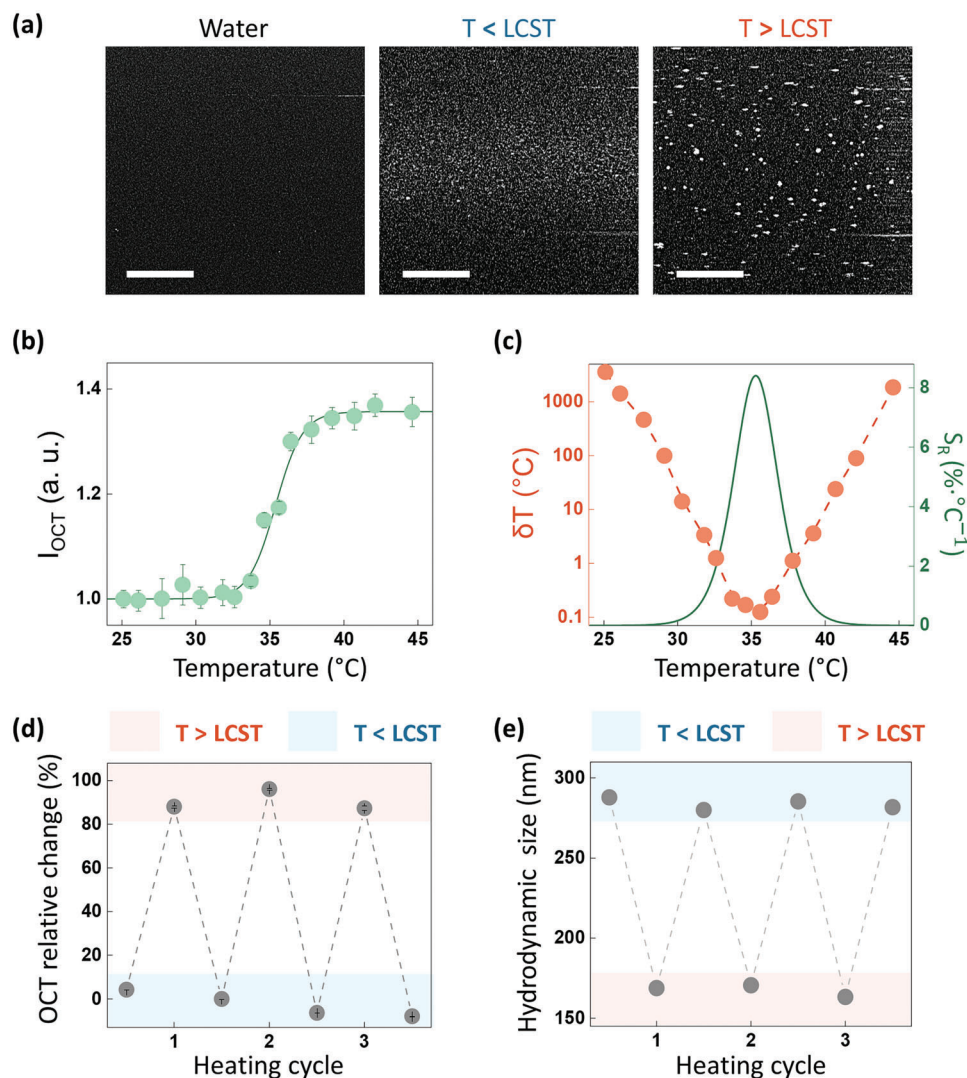


Figure 3. a) OCT images of an aqueous dispersion of PNIPAM-NGs with a concentration of 0.13 mg mL^{-1} in their swollen and collapsed state, that is, at temperatures below and above the LCST (20 and 45 $^{\circ}C$, respectively). An OCT image of pure water is included for comparison. Scale bars: 250 μm . b) Temperature dependence of the OCT contrast provided by PNIPAM-NGs in water. Dots are experimental data and the solid line is the best fit to a four-parameter sigmoidal function. c) Temperature dependence of the thermal sensitivity and thermal precision provided by PNIPAM-NGs. Dots are experimental data obtained from the analysis of the OCT images, and dashed lines are guides for the eyes. d) OCT contrast obtained below and above LCST after consecutive heating/cooling cycles. e) Hydrodynamic size of the PNIPAM-NGs nanogels after consecutive heating/cooling cycles. The error bars in (b,d) correspond to the standard deviation of the intensity of 10 consecutive OCT images.

(GNSs)—one of the most effective contrast agents for OCT—with $\sigma_{\text{scat}}(\text{GNSs@1300 nm}) = 6.9 \times 10^{-11} \text{ cm}^2$.^[17] Despite their relatively low scattering cross section, the PNIPAM-NGs nanogels dispersed in water are able to provide a clear OCT contrast in both their swollen and collapsed states (Figure 3a). The OCT intensity (I_{OCT}) generated by the PNIPAM-NGs dispersed in water increases up to 40% (from 1 to 1.4) with temperature and can be fitted to a four-parameter sigmoidal function (Figure 3b). The increase in the OCT signal with temperature is a direct consequence of the increase in the scattering cross section in accordance with previous works that have revealed that $I_{OCT} \propto \sigma_{\text{scat}}$.^[17] OCT contrast agents that do not undergo any structural phase transition (such as GNSs) were found to provide a signal that is temperature-independent (see Section

S5, Supporting Information).^[12a] Experimental data included in Figure 3b reveal the possibility of using PNIPAM-NGs for OCT with a relative thermal sensitivity ($S_R(T) = \frac{1}{I_{OCT}(T)} \frac{dI_{OCT}(T)}{dT}$) that reaches a maximum value of $8.4\% \text{ }^{\circ}C^{-1}$ at 35 $^{\circ}C$, that is, at the LCST (Figure 3c). The temperature precision achievable by OCT ($\delta T = \frac{1}{S_R(T)} \frac{\delta I_{OCT}(T)}{I_{OCT}(T)}$, where $\delta I_{OCT}(T)$ is the uncertainty in the OCT signal at temperature T) is concomitantly minimal (0.1 $^{\circ}C$) at the LCST (Figure 3c). On the other hand, the temperature precision deteriorates up to several degrees when the temperature deviates $\approx 5 \text{ }^{\circ}C$ from LCST (Figure 3c, Figure S7, Supporting Information), leading to erroneous thermal readouts at these temperatures. Thus, the operation range of PNIPAM-NGs as thermal sensors is narrow: a few degrees around the

LCST. The phase-transition temperature of the PNIPAM-NGs and, hence, their operation range can be shifted by modifying the structure of the polymeric chains to tune the LCST. Experimental data demonstrated that tuning the LCST to higher temperatures is possible but at the expense of a reduction in the maximum relative thermal sensitivity (Figure S6, Supporting Information). The reduced operation range of the PNIPAM-NGs hampers their use for certain applications such as tumor ablation monitoring, in which temperature increases of ≈ 20 °C can be achieved. Nevertheless, it does not limit their use in other applications in which smaller temperature fluctuations are involved such as thermal monitoring of moderate thermal treatments like diathermy (37–41 °C) and hyperthermia (41–48 °C), tissue diagnosis by using transient thermometry in which temperature variations of only a few degrees are required,^[18] and single cell thermal studies in which the intracellular temperature changes in response to external stimuli.^[19] Additionally, pre-clinical studies on in vivo murine models could directly benefit from the use of our proposed PNIPAM-NGs as thermal reporters since the core temperature under anesthesia is typically close to 35 °C.^[20]

Last, the robustness of the PNIPAM-NGs dispersed in water as thermal sensors was tested by recording the OCT contrast after consecutive heating and cooling cycles. The experimental results reveal the lack of hysteresis, which highlights the stability of the PNIPAM-NGs (Figure 3d). This is consistent with the reversibility of the hydrodynamic size values during consecutive heating/cooling cycles (Figure 3e). Additionally, in Section S3 (Supporting Information), we discuss the effect of pH and ionic strength of the dispersant buffer on the performance and properties of our PNIPAM-NGs. The ionic strength has a moderate impact on their LCST in the range tested. In typical physiological conditions, the ionic strength is 0.15 M and can suffer a fluctuation of ± 0.01 M.^[21] In those cases, the error in the measurement introduced by the variation of the LCST is $\approx \pm 0.09$ °C, which is smaller than the uncertainty of the measurement (0.1 °C as indicated in Figure 3c). Hence PNIPAM-NGs can be considered non-biased OCT probes.

The relatively low scattering cross section of the PNIPAM nanogels was still high enough to provide an OCT contrast when dispersed in water (i.e., a non-scattering medium). However, the results included in Figure 3 do not ensure that the PNIPAM-NGs would be able to provide a measurable OCT contrast in highly scattering media such as tissues. To explore this possibility, we analyzed the OCT contrast of the PNIPAM-NGs when they are homogeneously distributed in agar tissue phantoms (see the Experimental Section for more details of the preparation procedure). The presence of the PNIPAM-NGs clearly enhances the contrast in the OCT images of the tissue phantoms at room temperature, which further increases with temperature following a four-parameter sigmoidal function (see Figure S7b, Section S7, Supporting Information). When the PNIPAM-NGs are embedded in the phantom the sensitivity is slightly reduced to a value of 6.5% °C⁻¹, and the transition is broader with a full-width at half maximum of 3 °C, due to the interaction of the PNIPAM-NGs with the polymer chains of the tissue phantom. Interestingly, the minimal thermal uncertainty at the LCST remains unchanged (Figure S7c, Supporting Information). The unequivocal relation between I_{OCT} and tissue temperature suggests the possibility of

3D thermal imaging of tissues by OCT. To demonstrate this possibility, we have designed an experiment in which the tissue phantom embedding PNIPAM-NGs is illuminated by a focused (50 μm radius) 1450 nm wavelength laser (Figure 4a). Simultaneously, thermal images of the tissue phantom are acquired with an infrared thermal camera, which allows to check the correctness of the thermal readout provided by PNIPAM-NGs at the tissue surface (see Section S8, Supporting Information). The tissue phantom temperature is kept at 27 °C to ensure that the PNIPAM-NGs are within their temperature operating range (Figure 3c). This particular wavelength was used since the absorption coefficient of the tissue phantoms at 1450 nm is close to 30 cm^{-1} (Figure S9, Supporting Information), so the laser radiation is completely absorbed in a very short ($\approx 300\text{ }\mu\text{m}$) distance creating a well-localized thermal gradient in the surroundings of the laser spot.^[22] When the 1450 nm laser is off, the 3D OCT image of the tissue shows a homogeneous contrast that corresponds to a uniform temperature (Figure 4b). When the 1450 nm laser is turned on, the OCT intensity in the surroundings of the laser spot increases, revealing a local increase in the tissue temperature (Figure 4e). By using the calibration curve of Figure S7b (Supporting Information) it is possible to build the 3D thermal image shown in Figure 4c, following the procedure explained in Section S10 (Supporting Information). This 3D thermal image reveals a localized temperature increase (up to 15 °C) at the surface of the tissue. This becomes more evident in the xz cross-sectional thermal image included in Figure 4d, in which a thermal gradient extending up to a distance of 1 mm from the laser spot is observed. The experimental data included in Figure 4d agree with the cross sectional image obtained by numerical simulations of the bioheat transfer equation using 3D-finite difference calculations following the Douglas–Gunn method (Figure 4e).^[23] Details of the procedure followed for the numerical simulations are given in Section S11 (Supporting Information). The agreement between experimental data and numerical simulations becomes clear when the vertical and horizontal temperature profiles are compared (Figure 4f). Such a good agreement between experimental data and numerical simulations confirms the suitability of PNIPAM-NGs as reliable thermal reporters in OCT.

Figure 4 shows that the thermoresponsive PNIPAM-NGs incorporated within a tissue phantom enable the acquisition of 3D thermal images. However, achieving a homogeneous distribution of nanostructures within tissues in vivo is not feasible. In these cases, the most reliable approach is the injection of the thermal nanosensors into the tissue that will be thermally monitored. The ability of a well-localized injection of PNIPAM-NGs for the thermal monitoring of a tissue has been studied in a model of photothermal treatment of the brain (Figure 5a). In this model, we use a brain phantom that provides a similar OCT image to that of a real mouse brain (see Section S12, Supporting Information). Given their stability, agar phantoms are generally accepted as substitutes for real tissue for in vitro models of the mammalian brain.^[24] Phantoms allow us to overcome the problem of tissue dehydration when it is isolated from the animal, especially in experiments involving tissue heating. 2 μL of an aqueous dispersion of PNIPAM-NGs (6.7 mg mL^{-1}) were injected at a depth of 0.5 mm. This reduced volume reproduces the limitations imposed in in vivo experiments to keep intracranial pressure within safe limits.^[25] The brain phantom was then placed in the field of

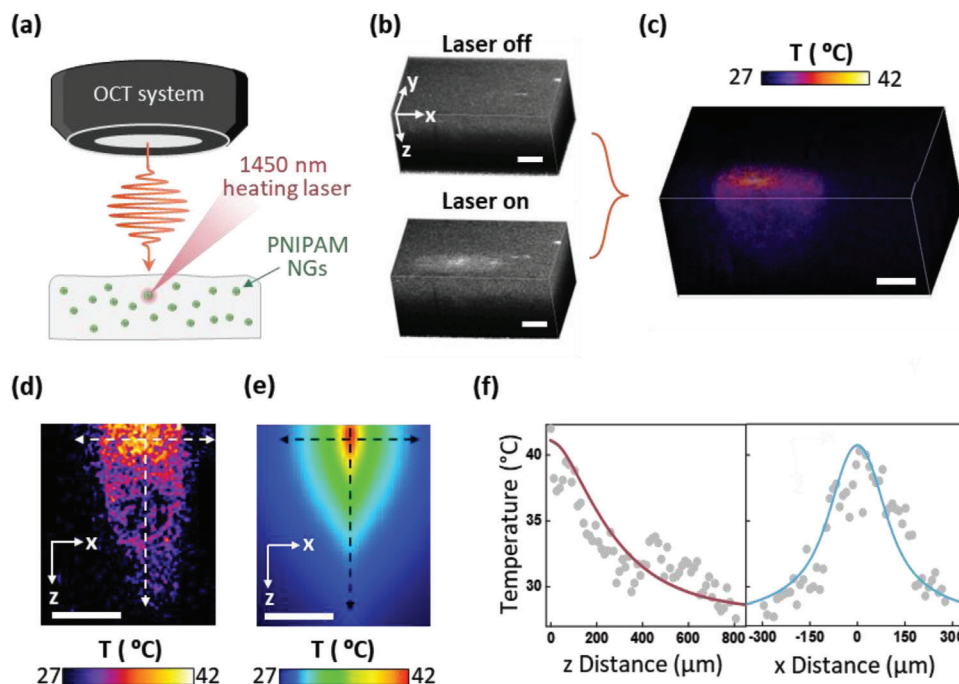


Figure 4. a) Schematic representation of the photothermal experimental designed to induce well-localized thermal gradients within tissues. b) 3D OCT images of a tissue phantom with a homogeneous distribution of PNIPAM-NGs in the absence (laser off) and presence (laser on) of 1450 nm focalized laser irradiation. c) Optical coherence thermometry image of a tissue phantom when irradiated by a focused 1450 nm laser radiation as obtained from the OCT images included in (b). d) Cross-sectional view of the thermal image in c) obtained for $y = 0$ that corresponds to the location of the laser spot. e) Numerically simulated cross sectional image of a tissue locally heated by a 1450 nm focused laser beam. f) Left: Temperature profile along the $(0,0,z)$ direction (vertical arrow in (d,e)). Dots are experimental data and solid line is obtained from numerical simulations. Right: Temperature profile along the $(x,0,0)$ direction (horizontal arrow in (d,e)). Dots are experimental data and solid line is obtained from numerical simulations. Scale bars: 250 μm .

view of the OCT system and illuminated with an expanded continuous wave 980 nm laser that triggers photothermia due to the tissue absorption at this wavelength.^[26] The superficial temperature of the tissue was monitored via infrared thermal imaging as shown in Figure S8 (Supporting Information). In the absence of the 980 nm laser, the PNIPAM-NGs were in their swollen state (below the LCST) so they provided low OCT contrast (see Figure 5b where the arrow indicates the location of the PNIPAM-NG injection). When the phantom brain is irradiated with the 980 nm laser for 3 min, photothermal conversion results in local heating of the brain that drives the PNIPAM-NGs to their collapsed state. Consequently, a clear enhancement of the OCT contrast occurs at the injection site (Figure 5c). Section S13 (Supporting Information) provides the OCT signal vs temperature of the region of the brain phantom where the PNIPAM-NGs are injected and also the evolution with a temperature of the intensity of the brain phantom. As seen in Figure S11 (Supporting Information), the intensity of the phantom remains unchanged, while the intensity of the PNIPAM-NGs injection increases up to 40%. Therefore, all the changes in the intensity obtained in the images are due to the structural changes in the PNIPAM-NGs. When the OCT image is converted into a thermal image, it is revealed that after 3 min of irradiation the temperature at the injection site has increased by $\approx 8^\circ\text{C}$ (Figure 5d). As it has been experimentally observed for other tissues, the laser-induced heating of the brain and any other tissue is not expected to be instantaneous.^[27] Indeed, the time evolution of the tissue temperature ($T_{\text{SC}}(t)$) during

the heating process is described by:

$$T_{\text{SC}}(t) = T_0 + \Delta T_{\text{max}} \times \left[1 + \left(\frac{1}{2\tau} - 1 \right) \operatorname{erf} \left(\sqrt{\frac{t}{\tau}} \right) - \sqrt{\frac{t}{\pi\tau}} \exp \left(-\frac{t}{\tau} \right) \right] \quad (3)$$

where τ is the characteristic thermal relaxation time, T_0 is the initial tissue temperature, and ΔT_{max} is the magnitude of laser heating. The characteristic thermal relaxation time is given by:

$$\tau = \frac{R^2}{4\alpha} \quad (4)$$

where α is the thermal diffusivity of the medium and R is the characteristic length of the heating process, i.e., the distance between the heating source and the heat sink (tissue–air interface). Fitting the thermal relaxation curves of tissues to Equation (3) has been widely used to access tissue properties and for diagnostic purposes.^[18] The analysis of the time-resolved OCT images reveals that the brain temperature increases monotonously with the irradiation time approaching asymptotically a steady state temperature (Figure 5e). The fit of these experimental data to Equation (3) gives $\tau = 80 \pm 20$ s. Since the thermal diffusivity of the tissue phantom used here is known ($\alpha = 0.15 \text{ mm}^2 \text{ s}^{-1}$), we can determine the characteristic length of the heating process $R = \sqrt{4\tau\alpha} = 7 \pm 1 \text{ mm}$. In our

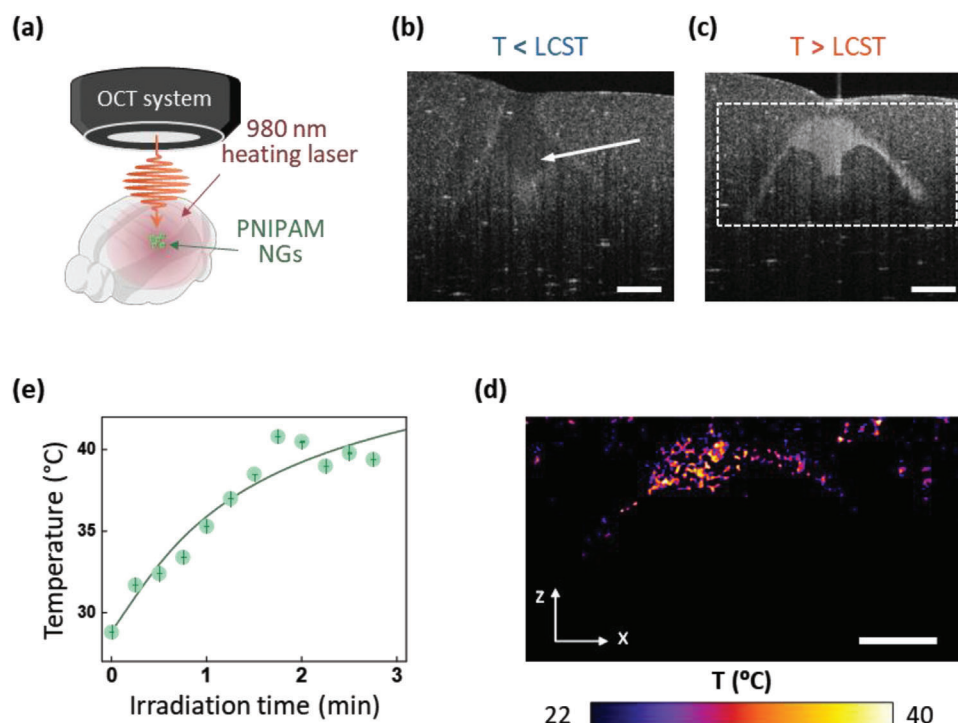


Figure 5. a) Schematic representation of the experimental setup used for mimicking a photothermal treatment of a brain with thermal feedback from PNIPAM-NGs and OCT. b) OCT image of the brain phantom in the absence of laser irradiation. The white arrow indicates the location of the injection of PNIPAM-NGs. c) OCT image of the brain phantom after 3 min of 980 nm irradiation. d) Thermal image of the dashed area indicated in c). Scale bars in all images: 250 μm . e) Time evolution of the brain phantom temperature determined from the analysis of the OCT images during the irradiation with a 980 nm laser. The dots are experimental data, and the solid line is the best fit to Equation (3) in the main text. The error bars have been calculated by the propagation of the error of the variables in Equation (3).

case, R can be assumed to be the penetration depth (l_p) of the 980 nm radiation that, in a first-order approximation, is equal to the inverse of the tissue extinction coefficient (α_{ext}) at 980 nm so that $l_p = R = 1/\alpha_{\text{ext}}$. Thus, the analysis of the heating curve yields us an extinction coefficient for our tissue phantom at 980 nm of $\alpha_{\text{ext}}(980 \text{ nm}) = 1.4 \pm 0.2 \text{ cm}^{-1}$ that is in good agreement with the extinction coefficient obtained experimentally from optical density measurements ($\alpha_{\text{ext}}(980 \text{ nm}) = 1.5 \text{ cm}^{-1}$, see Section S9,f Supporting Information).

In addition, even if the use of tissue phantoms constitutes a valid model for tissue imaging, we explored the possibility of performing OCT in animal tissue. As discussed in Section S14 (Supporting Information), a proof-of-concept experiment of photothermia in chicken muscular tissue was performed. A capillary filled with the PNIPAM-NGs dispersion was inserted in the tissue, and 3D thermal images of the capillary within the tissue were obtained after irradiation with a 980 nm laser for 3 min (Figure S12, Supporting Information).

3. Conclusion

We have demonstrated that 3D imaging and temperature sensing in tissues is possible using optical coherence thermometry based on OCT, a routinely used 3D clinical imaging technology. As thermal sensors, we employed PNIPAM polymeric nanogels that undergo a volume phase transition (polymer collapse) at $\approx 35^\circ\text{C}$. The polymer collapse increases the infrared scattering

efficiency of the PNIPAM nanogels so that their OCT contrast is temperature-dependent, providing maximum relative thermal sensitivities close to $8\% \text{ }^\circ\text{C}^{-1}$. This large thermal sensitivity is combined with the superior spatial resolution of OCT to build up 3D thermal images of tissues subjected to submillimeter local heating caused by a focused laser beam. A good agreement was found between the experimental data and the numerical simulations revealing the potential of optical coherence thermometry to monitor thermal effects at the microscale. The combination of PNIPAM nanogels and OCT was also used to provide thermal monitoring in a phantom model of laser-induced brain hyperthermia, revealing the potential of this approach for future clinical applications.

The results included in this work enable a direct translation of nanothermometry into the clinical world and demonstrate the feasibility of obtaining 3D thermal imaging of tissues by employing a conventional technology commonly used in clinics.

4. Experimental Section

Synthesis of PNIPAM Nanogels: The synthesis of the thermoresponsive nanogels was carried out using the free surfactant polymerization method.^[13a,28] Briefly, an aqueous solution (10 mL) containing *N*-isopropylacrylamide (0.1 M, 113 mg), sodium acrylate (0.05 M, 4.7 mg), and cross-linker *N,N'*-methylene bisacrylamide (0.05 M, 7.7 mg) was heated under N_2 atmosphere. When the temperature reached 70°C , the polymerization was started by adding 100 μL of 2,2'-azobis-

(2-methylpropionamide) (0.1 M, 2.7 mg). The reaction of the mixture was kept for 2 h, and after this time, the milky-like dispersion was cooled down, filtered, and dialyzed against distilled water for 2 days to remove unreacted monomers. Finally, the nanogels were collected by centrifugation at 15 000 RCF, redispersed in 10 ml of Milli-Q water, and stored at room temperature.

Electron Microscopy Images: To obtain the dimension and shape of synthesized nanogels, transmission and scanning electron microscopy (TEM and SEM respectively) imaging was performed. TEM images were taken by pouring a drop of 10 μL of a tenfold diluted dispersion of the synthesized nanogels on a TEM grid. Once the grid was dried, it was analyzed in a Jeol JEM 1010 microscope. In the case of the SEM images, these were obtained by placing a tenfold diluted dispersion of nanogels on a circular microscope glass cover. Subsequently, it was left to dry and metalized with gold to create a 3 nm conductive layer suitable for the SEM analyses. For the SEM study, a Jeol JSM 7600F was used and to increase the contrast of the sample, images were taken, tilting the sample holder 30°.

Hydrodynamic Size: The hydrodynamic size of the nanogels was determined by dynamic light scattering. A Malvern Zetasizer Nano ZS equipment (Malvern) was used, and the intensity size distributions of the dispersion were measured at temperatures from 20 to 50°C with a step of 2.5–5 °C. The equilibration time was 120 s, and the detection angle was 173° (backscattering). Three size distributions were recorded for each temperature. The value of the size of the nanogels for each temperature was calculated as the average position of the maximum distribution for the three measurements.

Extinction Spectra: The optical density (OD) of the dispersion of the PNIPAM nanogels was measured using a double-beam absorption spectrophotometer (Lambda1050, Perkin Elmer), covering a spectral range of 390 to 1340 nm and using a quartz cuvette with a path length of 2 mm. To control the temperature of the dispersion, a Peltier temperature controller (Q-pod 2e, Quantum Northwest) was placed inside the spectrophotometer. Measurements were taken in the 20–50 °C temperature range. To obtain the extinction coefficient (α_{ext}) and the extinction cross section (σ_{ext}) the following equation was used:

$$\alpha_{\text{ext}} = \frac{\text{OD}}{d \log(e)} = \sigma_{\text{ext}} N \quad (5)$$

where d is the path length of the cuvette (2 mm) and N is the concentration of particles in the dispersion expressed in particles per cm^3 .

Optical Coherence Tomography Images: OCT measurements were performed using a spectral domain tomograph (Thorlabs Telesto TEL321C1 OG-13) with a maximum working wavelength of 1300 nm (range 1250 to 1380 nm). The system was equipped with an LSM03 scan lens with a working distance of 25.1 mm. The axial scan rate was 92 kHz. The axial resolution in water was 4.9 μm , the lateral resolution was 13 μm , and the maximum imaging depth was 2.5 mm.

The analysis of the OCT images was performed using ImageJ software. For the calibration curves of the PNIPAM-NGs in dispersion or embedded in the tissue phantom, an intensity threshold was applied to all the images, so only the intensity from the NGs was registered. Then a region of interest was defined, and the intensity of the PNIPAM-NGs was calculated for each of the 10 frames of every OCT image. Finally, the normalized intensity and the OCT relative change were determined as:

$$\text{Norm } I_{\text{OCT}} = \frac{I_{\text{OCT}}(T)}{I_{\text{OCT}}(T_{\text{min}})};$$

$$\text{OCT relative change} = \frac{I_{\text{OCT}}(T) - I_{\text{OCT}}(T_{\text{min}})}{I_{\text{OCT}}(T_{\text{min}})} \quad (6)$$

I_{OCT} being the intensity of the region of interest, and T_{min} the lowest temperature recorded.

Tissue Phantom Preparation: Deionized water (7 mL) was added to an Erlenmeyer flask, submerged in an oil bath, and heated to 100 °C. When the water started to boil, the agar powder (1.25% w/v) was added and let dissolve under vigorous stirring for 20 min. Depending on the require-

ments of the phantom, two different procedures were followed: a) after 20 min of stirring, the temperature was reduced to 80 °C and 140 μL of PNIPAM nanogels (15 mg mL^{-1}) in water were added to the mixture to obtain a phantom with uniformly embedded nanogels with a final concentration of nanogels of 2% v/v. After 5 min the phantom was poured into a crystalizing dish and left to cool to room temperature for 2 h and then stored at 4 °C until further use; b) immediately after agar addition, intralipids (Sigma Aldrich, 20% emulsion) (1% v/v) previously dissolved in a small amount of ethanol were included in the mixture to obtain more realistic near-infrared scattering properties of the tissue. The gel was pipetted inside a self-designed mouse brain mold and stored at 4 °C until further use.

Temperature Control in OCT Images: A heating plate (Linkam Scientific CO102) with a precision of 0.1 °C was placed under the OCT scan lens. For obtaining images of the PNIPAM dispersions, a multi-well chambered coverslip (IBIDI μ -Slide 18 well polymer bottom – 81 811) was fixed over the heating plate, one of the wells was filled with 200 μL of the dispersion, and for recording the temperature, a thermocouple (TC-08 Data Logger, pico Technologies) was inserted into a nearby well filled only with water. To obtain images of tissue phantoms at different temperatures, a similar procedure was followed, this time placing the phantoms on a larger chambered coverslip (IBIDI μ -Slide 2 well glass bottom – 80 287).

For the photothermal treatment trials, a multimode high-power 980 nm laser (Laser Systems LIMO) was directed toward the brain phantom. The current reaching the laser was tuned so that the radiation power was 0.9 W. For thermal readouts in the brain phantom, a thermal camera (FLIR E54) was used.

Supporting Information

Supporting Information is available from the Wiley Online Library or from the author.

Acknowledgements

This work was financed by the Spanish Ministerio de Innovación y Ciencia under project NANONERV PID2019-106211RB-I00, NANOGRANZ PID2021-123318OB-I00, PID2020-118878RB-I00, RYC2021-032913-I, and TED2021-132317-I00B and under project COLUMNAS (PID2019-110632RB-I00), by the Instituto de Salud Carlos III (PI19/00565), by the Comunidad Autónoma de Madrid (S2022/BMD-7403 RENIM-CM and SI3/PJ1/2021-00211) and co-financed by the European structural and investment fund. Additional funding was provided by COST action CA17140, supported by COST (European Cooperation in Science and Technology) and the Fundación para la Investigación Biomédica del Hospital Universitario Ramón y Cajal (IMP21_A4 (2021/0427)).

Conflict of Interest

The authors declare no conflict of interest.

Data Availability Statement

The data that support the findings of this study are available from the corresponding author upon reasonable request.

Keywords

3D imaging, nanothermometry, optical coherence tomography (OCT), thermoresponsive nanogels

Received: February 25, 2023

Revised: June 4, 2023

Published online:

- [1] a) B. del Rosal, D. Ruiz, I. Chaves-Coira, B. H. Juárez, L. Monge, G. Hong, N. Fernández, D. Jaque, *Adv. Funct. Mater.* **2018**, *28*, 1806088; b) M. Xu, X. Zou, Q. Su, W. Yuan, C. Cao, Q. Wang, X. Zhu, W. Feng, F. Li, *Nat. Commun.* **2018**, *9*, 2698; c) H. D. A. Santos, E. C. Ximendes, M. d. C. Iglesias-de la Cruz, I. Chaves-Coira, B. del Rosal, C. Jacinto, L. Monge, I. Rubia-Rodríguez, D. Ortega, S. Mateos, J. GarcíaSolé, D. Jaque, N. Fernández, *Adv. Funct. Mater.* **2018**, *28*, 1803924; d) E. C. Ximendes, U. Rocha, B. del Rosal, A. Vaquero, F. Sanz-Rodríguez, L. Monge, F. Ren, F. Vetrone, D. Ma, J. García-Solé, *Adv. Healthcare Mater.* **2017**, *6*, 1601195.
- [2] a) X. Zhu, W. Feng, J. Chang, Y.-W. Tan, J. Li, M. Chen, Y. Sun, F. Li, *Nat. Commun.* **2016**, *7*, 10437; b) B. del Rosal, E. Carrasco, F. Ren, A. Benayas, F. Vetrone, F. Sanz-Rodríguez, D. Ma, Á. Juarranz, D. Jaque, *Adv. Funct. Mater.* **2016**, *26*, 6060.
- [3] Y. Leroy, B. Bocquet, A. Mamouni, *Physiol. Meas.* **1998**, *19*, 127.
- [4] S. Ueno, M. Hashimoto, H. Fukukita, T. Yano, in *IEEE Symp. on Ultrasonics*, IEEE, Piscataway, NJ, USA **1990**, pp. 1645–1652.
- [5] a) J. Zhou, B. del Rosal, D. Jaque, S. Uchiyama, D. Jin, *Nat. Methods* **2020**, *17*, 967; b) C. D. S. Brites, P. P. Lima, N. J. O. Silva, A. Millan, V. S. Amaral, F. Palacio, L. D. Carlos, *Nanoscale* **2012**, *4*, 4799.
- [6] L. R. Becerra, H. C. Breiter, M. Stojanovic, S. Fishman, A. Edwards, A. R. Comite, R. G. Gonzalez, D. Borsook, *Magn. Reson. Med.* **1999**, *41*, 1044.
- [7] L. Winter, E. Oberacker, K. Paul, Y. Ji, C. Oezderdem, P. Ghadjar, A. Thieme, V. Budach, P. Wust, T. Niendorf, *Int. J. Hyperthermia* **2016**, *32*, 63.
- [8] D. Silva, M. Sharma, R. Juthani, A. Meola, G. H. Barnett, *Neurosurgery Clinics* **2017**, *28*, 525.
- [9] D. Sung, P. A. Kottke, B. B. Risk, J. W. Allen, F. Nahab, A. G. Fedorov, C. C. Fleischer, *Commun. Phys.* **2021**, *4*, 68.
- [10] a) W. Drexler, U. Morgner, R. K. Ghanta, F. X. Kärtner, J. S. Schuman, J. G. Fujimoto, *Nat. Med.* **2001**, *7*, 502; b) A. G. Podoleanu, J. A. Rogers, D. A. Jackson, S. Dunne, *Opt. Express* **2000**, *7*, 292.
- [11] a) J. Men, Y. Huang, J. Solanki, X. Zeng, A. Alex, J. Jerwick, Z. Zhang, R. E. Tanzi, A. Li, C. Zhou, *IEEE J. Sel. Top. Quantum Electron.* **2016**, *22*, 120; b) H. G. Bezerra, M. A. Costa, G. Guagliumi, A. M. Rollins, D. I. Simon, *JACC Cardiovasc. Interv.* **2009**, *2*, 1035; c) J. Olsen, J. Holmes, G. B. Jemec, *J. Biomed. Opt.* **2018**, *23*, 040901; d) K. M. Au, Z. Lu, S. J. Matcher, S. P. Armes, *Adv. Mater.* **2011**, *23*, 5792.
- [12] a) J. Hu, F. Sanz-Rodríguez, F. Rivero, E. M. Rodríguez, R. A. Torres, D. H. Ortgies, J. G. Solé, F. Alfonso, D. Jaque, *Nano Res.* **2018**, *11*, 676; b) V. P. Nguyen, W. Qian, Y. Li, B. Liu, M. Aaberg, J. Henry, W. Zhang, X. Wang, Y. M. Paulus, *Nat. Commun.* **2021**, *12*, 34; c) T. Muñoz-Ortiz, J. Hu, F. Sanz-Rodríguez, D. H. Ortgies, D. Jaque, D. Méndez-González, R. Aguilar, F. Alfonso, F. Rivero, E. M. Rodríguez, J. García Solé, *Nanomedicine: NBM* **2022**, *43*, 102556.
- [13] a) J. Rubio Retama, B. Frick, T. Seydel, M. Stamm, A. Fernandez Barbero, E. López Cabarcos, *Macromolecules* **2008**, *41*, 4739; b) A. K. Teotia, H. Sami, A. Kumar, in *Switchable and Responsive Surfaces and Materials for Biomedical Applications*, (Ed: Z. Zhang), Woodhead Publishing, Oxford, UK **2015**; c) S. Hirotsu, I. Yamamoto, A. Matsuo, T. Okajima, H. Furukawa, T. Yamamoto, *J. Phys. Soc. Jpn.* **1995**, *64*, 2898.
- [14] a) H. Vihola, A. Laukkanen, L. Valtola, H. Tenhu, J. Hirvonen, *Biomaterials* **2005**, *26*, 3055; b) D. E. Meyer, B. C. Shin, G. A. Kong, M. W. Dewhirst, A. Chilkoti, *J. Controlled Release* **2001**, *74*, 213; c) A. Chilkoti, M. R. Dreher, D. E. Meyer, D. Raucher, *Adv. Drug Delivery Rev.* **2002**, *54*, 613; d) M. Ebara, M. Yamato, T. Aoyagi, A. Kikuchi, K. Sakai, T. Okano, *Biomacromolecules* **2004**, *5*, 505.
- [15] a) J. Wang, N. Huang, Q. Peng, X. Cheng, W. Li, *Mater. Chem. Phys.* **2020**, *239*, 121994; b) J. Litowczenko, J. Gapiński, R. Markiewicz, A. Woźniak, J. K. Wychowaniec, B. Peplińska, S. Jurga, A. Patkowski, *Mater. Sci. Eng. C* **2021**, *118*, 111507.
- [16] S. Hormeño, P. Gregorio-Godoy, J. Pérez-Juste, L. M. Liz-Marzán, B. H. Juárez, J. R. Arias-Gonzalez, *Small* **2014**, *10*, 376.
- [17] J. Hu, F. Rivero, R. A. Torres, H. Loro Ramírez, E. M. Rodríguez, F. Alfonso, J. García Solé, D. Jaque, *J. Biophotonics* **2017**, *10*, 674.
- [18] E. C. Ximendes, W. Q. Santos, U. Rocha, U. K. Kagola, F. Sanz-Rodríguez, N. Fernández, A. d. S. Gouveia-Neto, D. Bravo, A. M. Domingo, B. del Rosal, C. D. S. Brites, L. D. Carlos, D. Jaque, C. Jacinto, *Nano Lett.* **2016**, *16*, 1695.
- [19] C. Gota, K. Okabe, T. Funatsu, Y. Harada, S. Uchiyama, *J. Am. Chem. Soc.* **2009**, *131*, 2766.
- [20] K. L. Navarro, M. Huss, J. C. Smith, P. Sharp, J. O. Marx, C. Pacharinsak, *ILAR J.* **2021**, *62*, 238.
- [21] T. L. Lowe, S. G. Clarke, *J. Biol. Chem.* **2022**, *298*, 102290.
- [22] a) W. M. Piotrowski, R. Marin, M. Szymczak, E. Martín Rodríguez, D. H. Ortgies, P. Rodríguez-Sevilla, M. D. Dramićanin, D. Jaque, L. Marciniak, *Adv. Opt. Mater.* **2023**, *11*, 2202366; b) A. Sanchez-Cano, J. E. Saldaña-Díaz, L. Perdices, I. Pinilla, F. J. Salgado-Remacha, S. Jarabo, *Appl. Opt.* **2020**, *59*, D111.
- [23] J. Douglas, J. E. Gunn, *Numer. Math.* **1964**, *6*, 428.
- [24] a) R. Pomfret, G. Miranpuri, K. Sillay, *Ann. Neurosci.* **2013**, *20*, 118; b) M. Z. Vardaki, N. Kourkoumelis, *Biomed. Eng. Comput. Biol.* **2020**, *11*, 1179597220948100; c) G. Menikou, C. Damianou, *J. Ther. Ultrasound* **2017**, *5*, 14; d) G. McIlvain, E. Ganji, C. Cooper, M. L. Killian, B. A. Ogunnaike, C. L. Johnson, *J. Mech. Behav. Biomed. Mater.* **2019**, *97*, 65.
- [25] B. Mathon, M. Nassar, J. Simonnet, C. Le Duigou, S. Clemenceau, R. Miles, D. Fricker, *Neurosci. Bull.* **2015**, *31*, 685.
- [26] a) J. V. Frangioni, *Curr. Opin. Chem. Biol.* **2003**, *7*, 626; b) L. A. Sordillo, Y. Pu, S. Pratavieira, Y. Budansky, R. R. Alfano, *J. Biomed. Opt.* **2014**, *19*, 056004.
- [27] a) W. L. Nyborg, *Phys. Med. Biol.* **1988**, *33*, 785; b) F. J. Reynoso, C.-D. Lee, S.-K. Cheong, S. H. Cho, *Med. Phys.* **2013**, *40*, 073301; c) E. C. Ximendes, U. Rocha, K. U. Kumar, C. Jacinto, D. Jaque, *Appl. Phys. Lett.* **2016**, *108*, 253103.
- [28] M. Laurenti, E. López-Cabarcos, F. García-Blanco, B. Frick, J. Rubio-Retama, *Langmuir* **2009**, *25*, 9579.